Fabrication of Nitrogen-Doped Holey Graphene Hollow Microspheres and Their Use as an Active Electrode Material for Lithium Ion Batteries

Zhong-Jie Jiang*,[†] and Zhongqing Jiang[‡]

[†]New Energy Research Institute, College of Environment and Energy, South China University of Technology, Guangzhou 510006, Guangdong China

[‡]Department of Chemical Engineering, Ningbo University of Technology, Ningbo 315016, Zhejiang China

S *Supporting Information*

ABSTRACT: Nitrogen-doped holey graphene hollow microspheres (NHGHSs), synthesized through a template sacrificing method, were utilized as an anode material for lithium ion batteries (LIBs). Because of their specific microspherical hollow structure comprising nitrogen-doped holey graphene (NHG), the NHGHSs can exhibit reversible capacities of ~1563 mAh g^{-1} at a low rate of 0.5 C and ~254 mAh g^{-1} at a high rate of 20 C, which are significantly higher than the discharge capacity of the pristine graphene and other graphene-based carbonaceous materials. These, along with their good cycling stability, clearly demonstrate the great potential of using the NHGHSs as the anode material for LIBs of both high energy and power densities. We believe that the high specific surface area, holey structure of nitrogen-doped graphene, specific microspherical hollow structure, and increased interlayer spacing between the NHG nanosheets in their hollow walls are the main origins of their high electrochemical performance.

KEYWORDS: nitrogen doping, holey graphene, hollow microspheres, lithium ion batteries
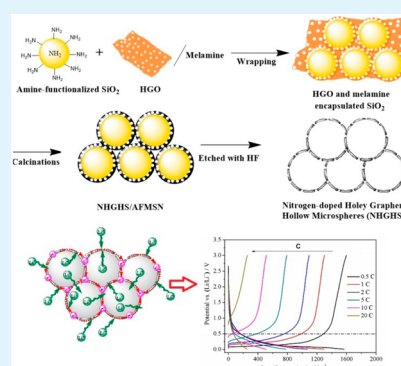
■ INTRODUCTION

Developing next-generation lithium ion batteries (LIBs) that are capable of delivering both high energy and power densities is of great interest for various technological applications, including portable electronic devices, electrical and plug-in hybrid electrical vehicles, etc.[1−3] Although the energy densities of LIBs might be improved through proper selection of electrode materials, the enhancement of their power densities remains a great challenge due to limited electron transfer and Li$^+$ ion diffusion rates in the electrode materials.[4−6] Great effort has been devoted to exploiting new materials or modifying the morphologies of the existing electrode materials to boost power densities of LIBs.[3,7−10] Since the power density of a LIB greatly depends on electron transfer and Li$^+$ ion migration rates through the electrode materials, approaches that are employed to improve the rate performance of the LIB include increasing the electrical and Li$^+$ conductivity of the electrode materials or developing electrode materials with a porous structure to reduce the path length of electrons and Li$^+$ ions that must migrate through during the charge/discharge process.[7,11]

Among various materials reported to date, graphene, which consists of a single planar of sp^2-bonded carbon atoms packed in a honeycomb crystal lattice, has attracted particular attention for uses in the applications of LIBs.[7,11−14] Its intrinsic properties, such as high in-plane electrical conductivity, excellent tensile modulus, and mechanical durability, make it highly attractive as the anode material for LIBs.[15−17] However,

the practical uses of graphene-based materials have revealed that the pristine graphene is prone to aggregation due to the strong van der Waals and π−π interactions between its graphitic planes of high surface area.[11,17,18] The aggregation would result in substantial loss of the active surface and generate discontinuous channels that retard fast ion transport, which greatly reduces the charge/discharge capacities of the graphene-based electrodes, especially at high charge/discharge rates.[7,11,18] In this case, although the in-plane Li$^+$ ion diffusivity of graphene is high (~10^{-8} cm^2 s^{-1}), its cross-plane diffusivity is low.[11] The intercalation of Li$^+$ ions in the graphene stack mainly occurs at the stack edge, while its intercalation into the underlying graphene in the stack has been greatly limited.[11,19,20]

Strategies that are frequently used to increase the electrochemical performance of the graphene-based carbonaceous materials include assembling them into a three-dimensional (3D) porous structure, introducing defects or holes to the basal plane of graphene, and doping of graphene with heteroatoms.[7,10,12,21−27] Since the porous structure can reduce the diffusion length of Li$^+$ ion migration during the charge/discharge process and allow more graphene accessible to the Li$^+$ ion storage, the graphene-based materials with a 3D porous structure would exhibit significantly improved electrochemical

performance over that of the pristine graphene, as demonstrated by the work reported previously.[7,21,28] The effects of point defects on the adsorption and diffusion of Li$^+$ ions on the graphene have been theoretically studied.[29−32] The results suggested that the presence of the defects would enhance the lithium adsorption on graphene, which has also been experimentally demonstrated by the improved electrochemical performance for the Li$^+$ ion storage of the disordered graphene nanosheets reported by Pan et al.[33] The introduction of holes would produce more defects into the basal plane of graphene. Therefore, the use of the holey graphene would greatly increase the electrochemical performance of the graphene-based carbonaceous materials as the anode materials for LIBs, since the holey graphene can not only produce more defects into the basal plane of graphene but also allows for the cross-plane diffusion of Li$^+$ ion through graphene and facilitates the formation of a 3D porous material.[10] The influence of the heteroatom doping on the electrochemical performance of graphene has been widely investigated theoretically and experimentally.[12,26,27,34] The doping can greatly increase the reactivity of the graphene-based materials and increase their adsorption energy and decrease their energy barriers for Li$^+$ ion penetration, due to hybridization of the heteroatom lone pair electrons with the graphene π system.[35,36] A great deal of work has shown that the heteroatom doped graphene exhibited significantly higher rate capacities and cycling stability than the pristine graphene and other graphene-based materials.[12,27,34,37,38]

The results mentioned above make us believe that a 3D porous material based upon nitrogen-doped holey graphene (NHG) would be of great interest as the anode material for LIBs, since the porous and nitrogen-doped holey structures could increase the electrochemical performance of the graphene-based material as the anode material for the LIB applications. To demonstrate this, we synthesize nitrogen-doped holey graphene hollow microspheres (NHGHSs) in this work through a template sacrificing method. The electrochemical results show that these NHGHSs can exhibit substantially high electrochemical performance when used as the anode material for LIBs, such as high energy and power densities, good reversibility, and excellent cycling stability. Their improved electrochemical performance could be attributed to the high specific surface area, holey structure of nitrogen-doped graphene (NG), specific microspherical hollow structure, and increased interlayer spacing between the NHG nanosheets in their hollow walls, all of which could increase rate capacities and cycling performance of the NHGHSs.

■ EXPERIMENTAL SECTION

Chemicals and Reagents. Flake graphite (325 meshes) was obtained from Alfa Ltd. Concentrated sulfuric acid (H$_2$SO$_4$, 95.0−98.0%), nitric acid (HNO$_3$, 65.0−68.0%), sodium nitrate (NaNO$_3$, ≥99.0%), potassium permanganate (KMnO$_4$, ≥99.5%), hydrochloric acid (HCl, 36.0−38.0%), hydrogen peroxide aqueous solution (H$_2$O$_2$, 30%), ethanol (CH$_3$CH$_2$OH, ≥99.5%), cetyltrimethylammonium bromide (CTAB, ≥99.0%), tetraethyl orthosilicate (TEOS), dimethyl sulfoxide (DMSO), and ethylene glycol (EG, ≥99.0%) were purchased from Shanghai Chemical Reagent Co. Ltd. 3-Aminopropyltriethoxysilane (APTES, ≥98.0%) was obtained from aladdin Co. Ltd. All the chemicals were used as received without further purification. Deionized (DI) water (H$_2$O) through Millipore system (Milli-Q) is used in all the experiments.

Preparation of Holey Graphene Oxide and Solution. The aqueous graphene oxide (GO) suspension (40 mL, 2 mg mL^{-1}),

obtained from the flake graphite by the modified Hummers method[39] (see Supporting Infomration for details), was mixed with concentrated HNO$_3$ (GO suspension/70% concentrated HNO$_3$ volume ratio of 1:5) in a sealed 500 mL conical flask under stirring. The mixture was ultrasonicated in a bath sonicator (100 W, 50/60 Hz) at room temperature for 1 h. After ultrasonication, the mixture was settled at room temperature for 1 h and poured into 100 mL of water. The obtained suspension was then centrifuged at 13 000 rpm and washed with water to remove the acid. The measurement showed that the holey graphene oxide (HGO) aqueous solution has a ζ-potential of −45.3 ± 0.37 mV.

Fabrication of the NHGHSs and the Nitrogen-Doped Graphene Hollow Microspheres (NGHSs). For the fabrication of NHGHSs, 0.3 g of amine-functionalized mesoporous silica nanoparticles (AFMSNs, the synthesis of which is given in Supporting Information) was first dispersed in 30.0 mL of distilled water. The pH value of the solution was then adjusted to 2.5 by adding a few drops of 1.0 M HCl solution. To this solution, 2.0 mg mL^{-1} negatively charged HGO suspension (15 mL) was added. The obtained mixture was stirred at room temperature for 24 h, which led to the wrapping of HGO onto AFMSNs through an electrostatic interaction. After that, 2.0 g of melamine was added into the above HGO-wrapped AFMSN (HGO/AFMSN) solution, and the mixture was stirred again at room temperature for 24 h before it was moved to an oven at 60 °C for 24 h. Through hydrogen bonding between the amine groups in the melamine and the oxygenous groups in HGO, ionic bonding between protonated amines and carboxyls, π−π interaction between unoxidized area in HGO and triazine rings, melamine could adsorb onto the surface of HGO/AFMSN particles. For the doping of N into the graphitic structure of graphene, the melamine-adsorbed HGO/AFMSN particles were placed in an alumina crucible in a horizontal furnace under a pure nitrogen gas atmosphere, heated to 800 °C with a heating rate of 5 °C min^{-1}, and then calcinated for 1.5 h. The obtained product was cooled to room temperature and doubly washed with a 10 wt % aqueous HF solution to remove the silica template. The final product was washed thoroughly with an acetone−water mixture and then with deionized water until the conductivity of the filtrate reached 10 μS. The synthesis of the NGHSs was accomplished using a procedure similar to the one used for the synthesis of the NHGHSs, while in the use of GO solution as precursor.

Materials Characterizations. The structure of the obtained GO and HGO was characterized by Fourier transform infrared spectroscopy (FTIR, PerkinElmer Spectrum BX FTIR instrument). An environmental scanning electron microscope (Model Quanta 650 FEG) at an operation voltage of 20.0 kV was used to measure the morphology of the obtained samples. TEM measurements were conducted on a JEM-2100F high-resolution transmission electron microscope with an accelerating voltage of 200 kV. For TEM characterization, the samples were first sonicated in ethanol (∼0.02 mg mL^{-1}) for 10 min, and then a droplet of the dispersions was cast onto a TEM copper grid followed by drying at room temperature. The ζ-potential measurements of materials were conducted on a Zetasizer Nano series (Malvern Instruments Ltd.). The chemical composition of the samples were determined by X-ray photoelectron spectroscopy (XPS) on a VG ESCALAB 250 spectrometer (Thermo Electron, U.K.), using an Al Kα X-ray source (1486 eV). The Raman spectroscopic measurements were carried out on a Raman spectrometer (Renishaw Corp., U.K.) using a He/Ne laser with a wavelength of 514.5 nm under ambient conditions, with a laser spot size of ∼1 μm. The X-ray diffraction (XRD) analysis was performed on a D/Max-III (Rigaku Co., Japan) using Cu Kα radiation and operating at 40 kV and 30 mA. The 2θ angular regions between 5° and 80° were explored at a scan rate of 2° min^{-1}. The specific surface areas of the samples were analyzed by a surface area analyzer (NOVA 2000, Quantachrome) using physical adsorption/desorption of N$_2$ at the liquid-N$_2$ temperature. Specific surface area was calculated according to the Brunauer−Emmett−Teller (BET) method. To measure the volumetric capacity density of the NHGHSs, their tap density was detected with a 100 mL measuring cylinder.[12,40] Typically, a small amount of the NHGHSs was first put into the measuring cylinder,
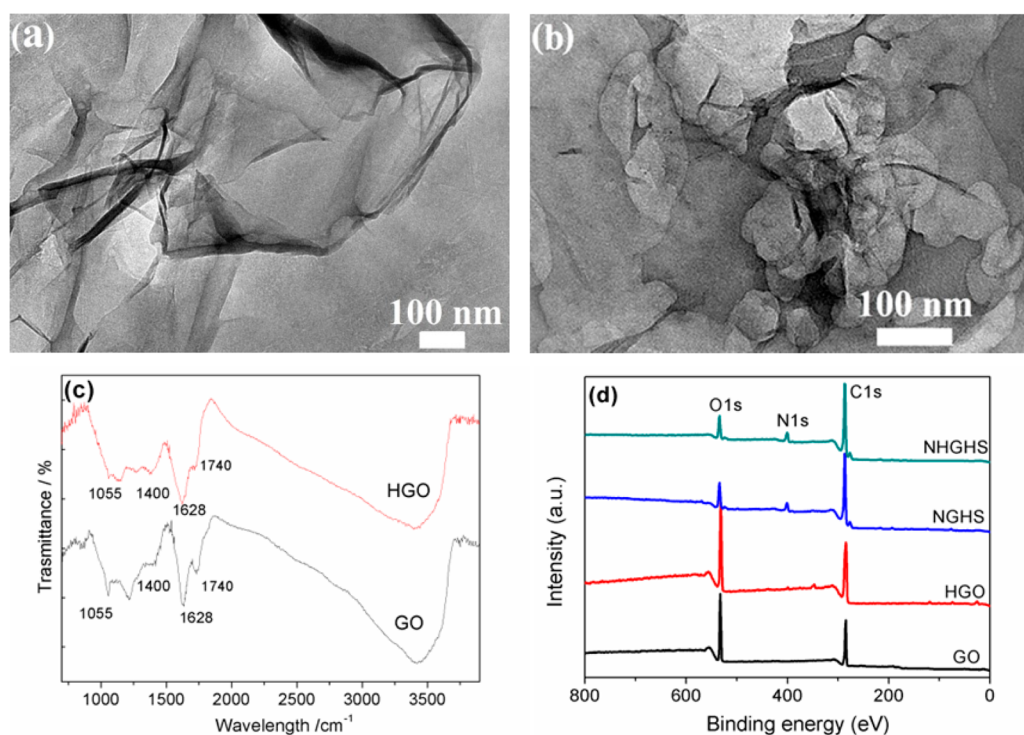
Figure 1. TEM images of (a) GO and (b) HGO. (c) FTIR spectra of GO and HGO. (d) XPS survey spectra of GO, HGO, NGHSs, and NHGHSs.

which was then knocked lightly at least 200 times until the NHGHS volume remained unchanged. To improve the accuracy of the tap density, several samples with different masses were measured, which gave the NHGHSs with a tap density of ~0.042−0.045 g cm^{-3}.

Electrochemical Measurements. Working electrodes were prepared by mixing 80 wt % active material (NGHSs or NHGHSs), 10 wt % acetylene black (Super-P), and 10 wt % polyvinylidene fluoride binder dissolved in N-methyl-2-pyrrolidinone. After coating the above slurries on Cu foils to form a thin film with thickness of ~15 μm, the electrodes were dried at 120 °C under vacuum for 2 h to remove the solvent before pressing. The thin film on Cu foil was then cut into round disks of 12 mm in diameter, which were dried at 100 °C for 24 h under vacuum and used as anodes for the coin cells. The amount of active material loaded onto the electrode film was ~1 mg cm^{-2}. The Li/NHGHS cells were assembled in an argon-filled glovebox with less than 1 ppm of oxygen and water, using lithium metal as the counter/reference electrode, a Celgard 2400 membrane separator, and 1 M LiPF$_6$ electrolyte solution dissolved in a mixture of ethylene carbonate and dimethyl carbonate (1:1 v/v). CR2032 (3 V) coin-type cells were used for electrochemical measurements. Galvanostatic charge−discharge cycles were tested by a LAND CT2001A electrochemical workstation at various current densities of 0.5 to 20 C between 3.0 and 0.01 V versus Li$^+$/Li at room temperature. The electrochemical impedance spectroscopy (EIS) was carried out by applying a perturbation voltage of 5 mV in a frequency range of 0.01 Hz to 100 kHz after the first discharge/charge cycle, using a Zahner IM6 electrochemical workstation.

■ RESULTS AND DISCUSSION

The NHGHSs were fabricated through a procedure involving the synthesis of graphene oxide (GO), the ultrasonication of the GO aqueous suspension in the presence of HNO$_3$ to get holey graphene oxide (HGO), the adsorption of HGO onto the surface of amine-functionalized mesoporous silica (AFMSNs), the calcinations of HGO wrapped AFMSNs (HGO/AFMSNs) in the presence of melamine, and the subsequent removal of AFMSNs by means of the HF etching. For the synthesis of GO, a modified Hummers method[39] was employed (see Supporting

Information), which produced GO with a sheetlike structure, as shown in Figure 1a. The FTIR spectra in Figure 1c indicates the presence of carboxyl, hydroxyl, and epoxy oxygen groups on GO, as demonstrated by its strong absorption bands at 3400, 1740, 1628, 1400, and 1055 cm^{-1}, corresponding to the O−H stretching, C=O stretching, adsorbed water, C−O deformation, and C−O stretching vibrations, respectively. The ultrasonication of GO in the presence of HNO$_3$ produced in-plane holes in the basal plane of GO. The TEM images in Figure 1b show that the ultrasonication in the presence of HNO$_3$ does not change the sheetlike structure of GO but produces in-plane holes in its basal plane, which can be clearly manifested by comparison of its TEM image with that of the parent GO shown in Figure 1a. These in-plane holes are formed due to the combining result of the continuous ultrasonication and the HNO$_3$ etching. Since the ultrasounds at the high acoustic pressures generated under the continuous ultrasonication would produce cavitation bubbles, which create high strain rates in the surrounding liquid upon implosion, the thusly generated frication forces between the moving liquid and GO could stretch and damage the carbon framework of GO.[41−44] With the help of ultrasonicating power, HNO$_3$ can attack the coordinatively unsaturated carbon atoms at the damage and existing edge sites of GO, resulting in partial detachment and removal of carbon atoms from the GO sheet and eventually producing GO with a holey structure. Indeed, as reported previously,[11,42,44,45] the technique in combination of the ultrasonication and the strong acid etching has been widely used for the generation of defects on carbonaceous materials and the scissoring of them into small pieces. Figure 1c shows that HGO exhibits a FTIR spectrum that is comparable to GO, suggesting that HGO and GO possess a similar elemental composition and are terminated with the similar oxygenous groups, such as carboxyl, hydroxyl, and epoxy oxygen groups. This can be demonstrated by their XPS spectra. As shown in
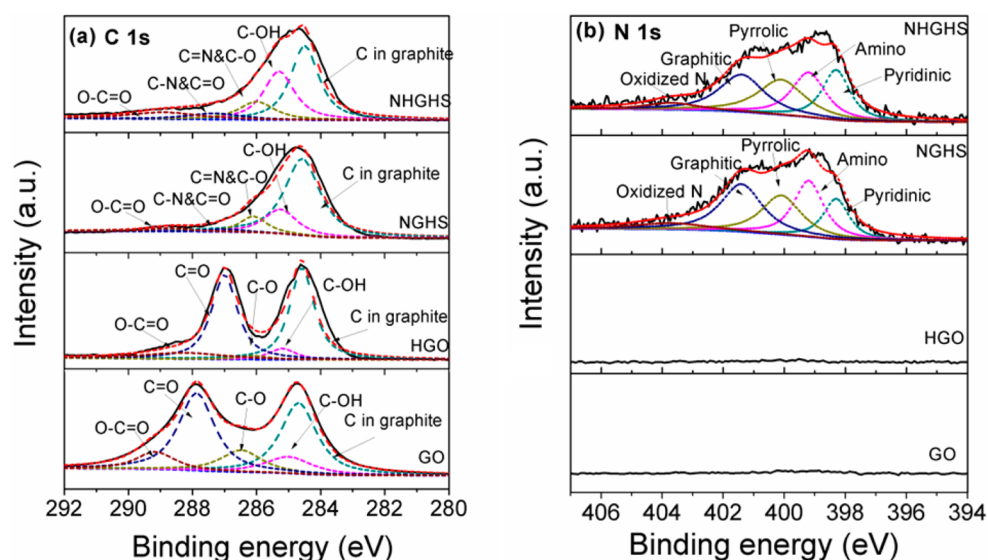
Figure 2. High-resolution XPS spectra of (a) C 1s and (b) N 1s for GO, HGO, NGHSs, and NHGHSs.

Figure 1d, in both GO and HGO, only elemental C and O are detected, while the spectra deconvolution of both C 1s spectra shows the presence of five different carbon oxidation states at binding energy of 284.7, 285.0, 286.4, 287.9, and 289.1 eV, corresponding to graphitic C, C−OH, C−O, C=O, and O−C=O, respectively (Figure 2a). The relative contents of C, N, and O in the GO and HGO are shown in Table 1. The slightly

Table 1. Relative Contents of C, N, and O in the GO, HGO, NGHS, and NHGHS Samples

samples	C 1s [atom %]	N 1s [atom %]	O 1s [atom %]
GO	40.52	0	59.48
HGO	39.43	0	60.57
NGHS	76.27	9.37	14.36
NHGHS	75.09	9.63	15.28

increased relative elemental contents of O in HGO compared to that in GO (as shown in Table 1) could be ascribed to the oxidation of some coordinatively unsaturated carbon atoms at the damage and existing edge sites of GO by HNO_3 during the ultrasonication and HNO_3 etching step, which produces more oxygenous groups in HGO. Because of the presence of the carboxyl, hydroxyl, and epoxy oxygen groups, HGO is negatively charged with a ζ-potential of -45.3 ± 0.37 mV, making it readily absorbable to the surface of positively charged AFMSNs (the ζ-potential of AFMSNs is 35.27 ± 0.47 mV) through an electrostatic interaction. The slightly more negative ζ-potential of HGO compared to GO could be attributed to its presence of more oxygenous groups (the ζ-potential of GO is -43.7 ± 0.42 mV), as demonstrated above. Supporting Information, Figure S1 shows the typical SEM image of HGO/AFMSNs. The NHGHSs can then be obtained through the calcination of HGO/AFMSNs in the presence of melamine and the subsequent removal of mesoporous silica templates. Figure 3a shows the typical SEM image of the NHGHSs, in which their microspherical hollow structure can be clearly visualized, indicating that most of the NHGHSs can remain the microspherical hollow morphology even after the template removal. This could be attributed to the multilayered nature of
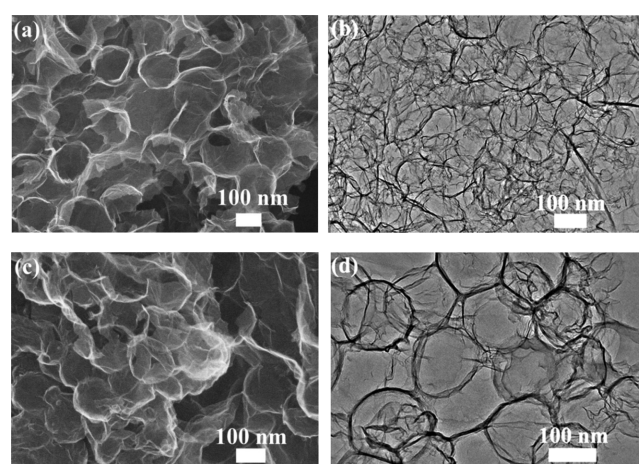

Figure 3. SEM and TEM mages of NHGHS (a, b) and NGHS (c, d).

the NHGHSs walls, making the microspherical hollow structure relatively stable. The multilayered nature of the NHGHS walls can be demonstrated by their TEM image shown in Figure 3b, which shows that the thicknesses of the NHGHS walls are much larger than 0.34 nm, the thickness of a single layer of graphene. However, contrary to the result shown in Figure 3a, the microspherical hollow structure of most of the NHGHSs was destructed in the TEM image (Figure 3b), indicating that the ultrasonication of the sample before its preparation for the TEM imaging could destroy the microspherical hollow structure of NHGHSs. This might be due to the lower interlayer interaction of the NHG nanosheets in the NHGHS walls, because its specific holey structure increases the pliability of the graphitic plane and decreases the $\pi-\pi$ interlayer interactions between nanosheets due to the reduction of the number of the conjugated carbons. This is unlike the NGHSs (synthesized from the unholey GO by the similar synthetic procedure used for the synthesis of NHGHSs, see the Experimental Section), fabricated by the similar synthetic procedure, whose TEM image exhibits a well-defined microspherical hollow structure even after an extended ultrasonication before the sample preparation for the TEM imaging (Figure 3d), because of the strong interlayer interaction of the
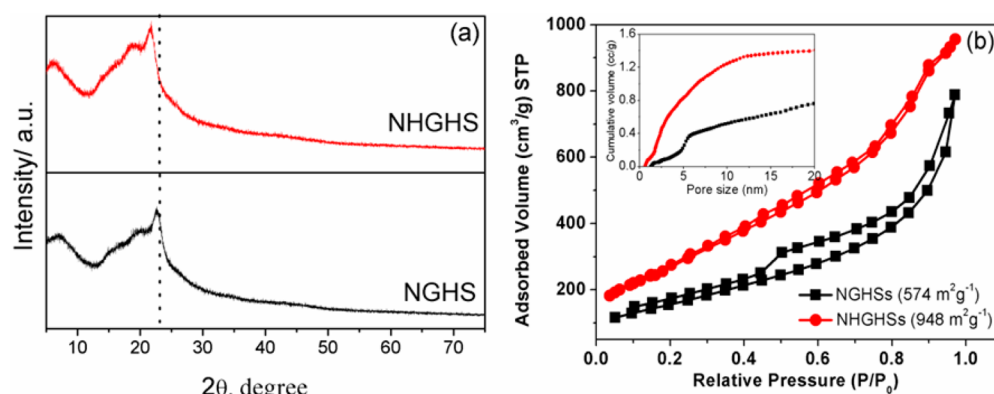
Figure 4. (a) XRD patterns of the NGHSs and NHGHSs. (b) N_2 adsorption−desorption isotherms of the NGHS and NHGHS. The specific surface areas of the samples were calculated using the Brunauer−Emmett−Teller (BET) method with the adsorption data at the relative pressure (P/P_o) range of 0.05−0.20. (inset) The cumulative pore volumes of the NGHS and NHGHS calculated using a slit/cylindrical NLDFT model.

Table 2. N 1s and C 1s XPS Elemental Analysis of the GO, HGO, NGHS, and NHGHS Samples

samples	N 1s [atom %]				C 1s [atom %]				
	pyridinic N	pyrrolic N	graphitic N	amino N	sp^2 C	C−OH	C−O/C=N^a	C−N/C=O^a	−O−C=O
GO					32.19	11.17	12.97	32.79	10.88
HGO					42.00	5.56	2.22	40.68	9.53
NGHS	15.63	23.14	29.42	24.86	65.13	19.11	10.39	2.44	2.94
NHGHS	21.12	24.95	25.51	23.00	41.24	29.54	12.89	6.62	9.71

^{a}For GO and HGO, there exist no C=N and C−N.

NG nanosheets in the NGHS walls due to the absence of holes in the basal plane of NG synthesize from the unholey GO, as shown in Figure 1a.

The low interlayer interaction between the NHG nanosheets in the NHGHS walls could also be demonstrated by their XRD pattern in Figure 4a. As shown in Figure 4a, the XRD pattern of the NHGHSs exhibits a peak at $2\theta = 21.6°$, which is close to the (001) reflection of the pristine graphene reported previously,[46] indicating that there exists the layered graphitic structure in the NHGHSs with an interlayer spacing of 0.41 nm. This is consistent with the TEM result shown in Figure 3b that the walls of the NHGHSs are multilayered. Although the NGHSs exhibit a XRD pattern similar to the NHGHSs, their diffraction peak appears at the relatively larger diffraction angle $(2\theta = 22.6°)$, suggesting that the NGHSs also possess a layered structure in the walls of their microspherical hollow structure but with the interlayer spacing smaller than that in the NHGHS walls. The larger interlayer spacing in the NHGHS walls implies a reduced interlayer interaction between the NHG nanosheets due to the decrease in the number of the conjugated carbon atoms in their basal plane. This clearly explains why the microspherical hollow structure of the NHGHSs would be destroyed after the ultrasonication procedure due to the relatively lower interlayer interaction between the NHG nanosheets, while the NGHSs can remain their microspherical hollow structure even after the extended ultrasonication due to the strong interlayer interactions between the NG nanosheets, although the SEM images of both NGHSs and NHGHSs exhibit the well-defined microspherical hollow structure with no distinguishable differences observed, as shown in Figure 3a,c.

The presence of N in the NHGHSs can be clearly demonstrated by their XPS spectrum displayed in Figure 1d. As shown in Figure 1d, except for the elemental O and C, which are initially present in the HGO used for the synthesis of the NHGHSs, the NHGHSs also exhibit a new peak

corresponding to N, indicating that the elemental N has been intercalated into the NHGHSs. The greatly reduced relative contents of O in the NHGHSs compared to that in HGO (Table 1) strongly suggests that the majority of oxygenous groups has removed through their reactions with melamine or decomposed during the high-temperature calcinations. Quantitative elemental analysis shows that the relative elemental percentage of N in the NHGHSs is 9.63% (Table 1), which is slightly higher than that in NGHSs (9.37%). This is in good agreement with the results shown above that HGO are terminated with more oxygenous groups, which would give NHGHSs with a higher N percentage, since the intercalation of N into carbonaceous materials proceeds mainly through the reactions of N-containing precursors with the oxygenous groups in the oxidized counterpart of graphene.[12,34,47] To unravel the oxidation states of elemental N in the NHGHSs, the spectra deconvolution of N 1s peak is done, as shown in Figure 2b. It indicates that there are five different components of nitrogen-containing groups in the NHGHSs, corresponding to pyridinic (398.3 eV), amine (399.2 eV), pyrrolic (400.1 eV), graphitic (401.4 eV), and oxidized (403.7 eV) type N-functionalities, respectively. Although the spectra deconvolution of N 1s of the NGHSs also shows the presence of five different components of nitrogen-containing groups, corresponding to pyridinic, amine, pyrrolic, graphitic, and oxidized type N-functionalities (Figure 2b), their relative contents are indeed different from those in the NHGHSs, as shown in Table 2. This could be attributed to the differences in the relative contents of the oxygenous groups between GO and HGO that are used for the synthesis of NGHSs and NHGHSs, respectively, as demonstrated by their deconvoluted spectra of C 1s shown in Figure 2a and the elemental analysis results shown in Table 2. Since the incorporation of elemental N into the graphitic structure is facilitated by the oxygenous groups, the differences in the form of the oxygenous groups would
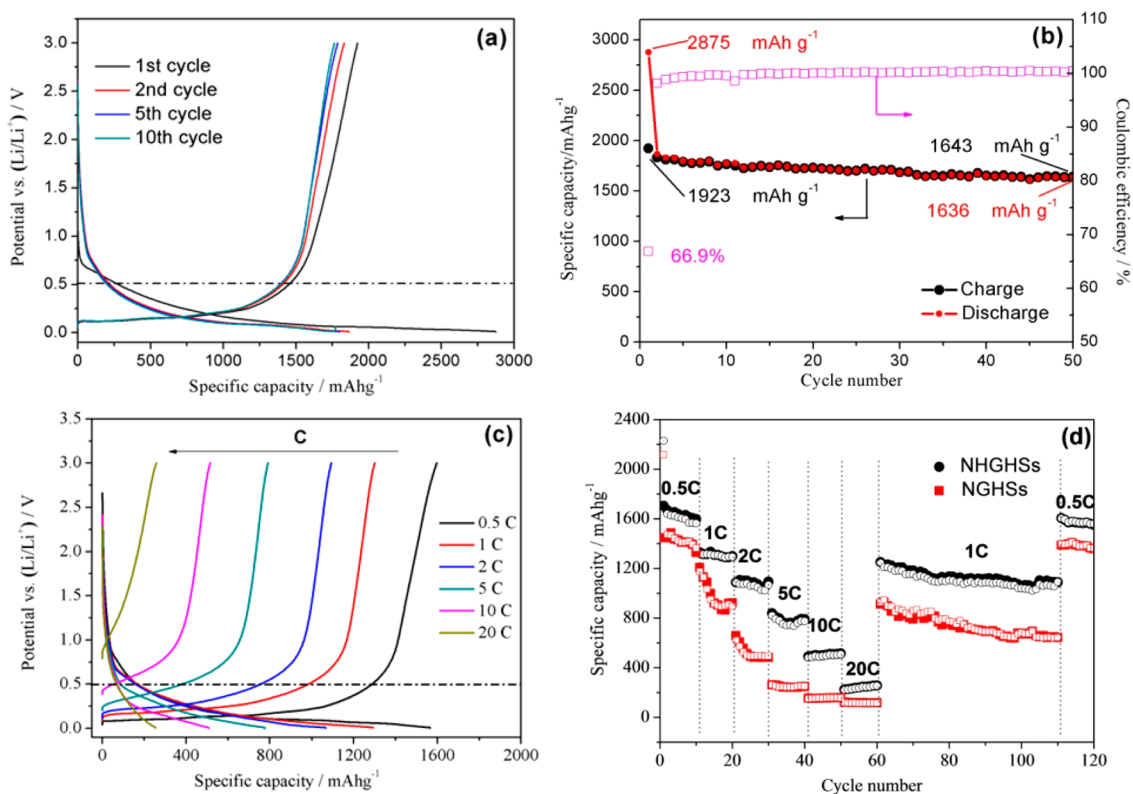
Figure 5. (a) Galvanostatic discharge−charge profile and (b) cycle performance and Coulombic efficiency of the NHGHS electrode at a low current rate of 100 mA g^{-1} between 3.0 and 0.01 V vs Li$^+$/Li. (c) Galvanostatic discharge−charge profiles of the NHGHSs at the different discharge/charge rates. (d) Rate capabilities and cycle performance of the NHGHSs and the NGHSs obtained over a wide range of high current densities from 0.5 to 20 C. The solid dots and squares correspond to the discharge capacities, while the circles and hollow squares correspond to the charge capacities.

produce the N-containing components with the different oxidation states. Additionally, the spectra deconvolution of C 1s also shows the dominance of the graphitic C in the NHGHSs (Figure 2a), suggesting that the NHGHSs possess a graphitic structure. This is further supported by their Raman spectrum shown in the Supporting Information (Figure S2), where two prominent peaks corresponding to the characteristic G (corresponding to the first-order scattering of the stretching vibration mode E$_{2g}$ of sp^2 carbon domains) and D (arising from the disordered carbon at the edge and defect sites and other defects oriented sp^3 bonded carbons such as dangling bonds, vacancies, and so on) bands[12,38] of the graphitic structure can be clearly visualized. The greatly increased intensity ratio of D band to G band (I_D/I_G = 1.36) of NHGHSs, compared to those of GO (I_D/I_G = 1.12), HGO (I_D/I_G = 1.14), and NGHSs (I_D/I_G = 1.17), suggests that the existence of the intercalated N and in-plane holes in the basal plane of NHG and their specific microspherical hollow structure would produce more disordered carbon atoms in the NHGHSs.

Because of their specific microspherical hollow structure, the NHGHSs exhibit a specific surface area as high as 948 m^2 g^{-1}, as demonstrated by their N$_2$ adsorption−desorption isotherms shown in Figure 4b. Although the specific surface area of the NHGHSs is still lower than the theoretical specific surface area of the single-layer graphene nanosheet (~2600 m^2 g^{-1}),[48] it is much larger than those of the conventional graphene-based materials (usually lower than 500 m^2 g^{-1}),[49,50] in which the strong π−π and hydrophobic interactions between the graphitic planes lead them to lower specific surface areas due to layer-by-layer intimate stacking of the graphene nanosheets. Most

interesting is that the specific surface of the NHGHSs is much larger than that of the NGHSs (574 m^2 g^{-1}) in spite of the similarity of the microstructure between the NHGHSs and NGHSs. This suggests that the presence of the in-plane holes in the basal plane, which increases the interlayer spacing of NHG in the walls of the hollow structure of the NHGHSs, could make more NHG accessible to the N$_2$ adsorption. This might be a fascinating feature for the application of the NHGHSs in LIBs, since their increased specific surface area could render more active sites accessible to the Li$^+$ ion adsorption.

To evaluate the electrochemical performance of the NHGHSs as the anode for LIBs, their galvanostatic discharge/charge behaviors in the potential range from 3.0 to 0.01 V at a rate of 100 mA g^{-1} were measured. Figure 5a shows that the discharge/charge curves of the NHGHSs exhibit no voltage plateaus, due to the presence of a large amount of disordered carbon atoms (as demonstrated by the Raman spectrum shown in Supporting Information, Figure S2), which make the Li$^+$ ion adsorption sites electrochemically and geometrically nonequivalent in the NHGHSs. The first discharge/charge cycle reveals that the initial specific discharge and charge capacities of the NHGHSs are 2875 and 1923 mAh g^{-1}, respectively, which give an initial Coulombic efficiency of 66.9%. The irreversible capacity loss in the initial discharge/charge cycle could be attributed to the formation of solid electrolyte interphase (SEI) layer at the surface of the NHGHS electrode, the electrolyte decomposition, and/or the reaction of lithium ions with the residual oxygen-containing functional groups.[12,18,51] Because of these undesired processes, the specific discharge and charge capacities of the NHGHSs are greatly
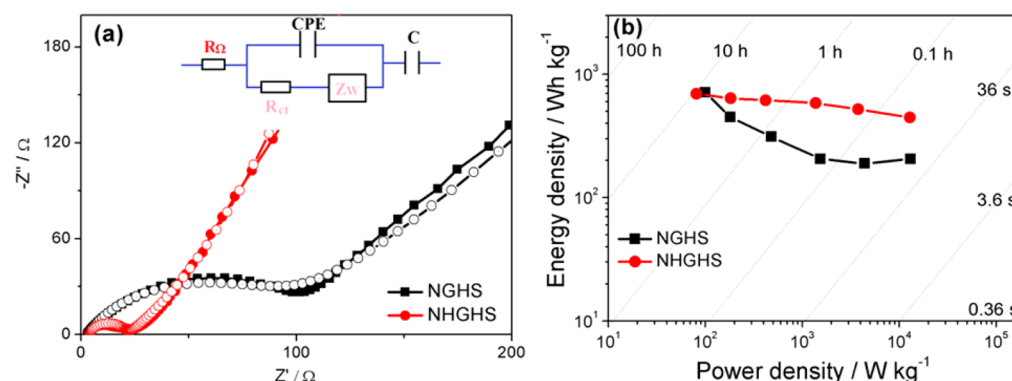
Figure 6. (a) Nyquist plots of the NHGHSs and the NGHSs. The solid dots and squares refer to the experimental data, while the circles and hollow squares correspond to the fitted data based on an equivalent circuit shown in the inset. In the plot, R_Ω stands for the electrolyte resistance, R_{ct} indicates the charge transfer resistance, Z_W is the "Warburg"-type element related to Li ion diffusion, CPE is the constant phase element, and C is the potential-dependent capacitance. (b) Ragone plots for the NHGHS- and NGHS-based cells with lithium metal as the counter/reference electrode. The calculations of gravimetric energy and power densities were based on the active material mass of a single electrode.

reduced in the second discharge/charge cycle, as shown in Figure 5a,b. The Coulombic efficiency of the second discharge/charge cycle is 98.2%, which is further increased to 100.0% in the fifth discharge/charge cycle, indicating an improved reversibility of the Li$^+$ ion intercalation and detercalation stability after the initial discharge/charge cycle. This could also be demonstrated by the similarity of the fifth and 10th discharge/charge profiles shown in Figure 5a and the near unit Coulombic efficiency after the initial several discharge/charge cycles shown in Figure 5b.

Compared to the discharge/charge capacities of most graphene-based or other nitrogen-doped graphene materials,[11,12,34,51] the discharge/charge capacities of the NHGHSs reported in this work are much higher, indicating the superiority of using the NHGHSs as the anode material for the LIB applications. To further demonstrate the superiority of the NHGHSs as the anode material for the LIB applications, their electrochemical performance at the different discharge/charge rates is measured. Figure 5c shows that the NHGHSs can deliver reversible specific capacities of 1580, 1308, 1068, and 776 mAh g^{-1}, respectively, at the current rates of 0.5, 1, 2, and 5 C. Even at the significantly high discharge/charge rates of 10 and 20 C, the NHGHSs can still deliver reversible respective specific capacities of 507 and 254 mAh g^{-1}. These reversible capacities are significantly higher than those of most graphene-based or other NG materials,[3,11,34,38] clearly demonstrating that the NHGHSs are the promising anode material for LIBs with high energy and power densities. In addition, the NHGHSs also exhibit excellent cycling stability at the high discharge/charge rates. As shown in Figure 5d, except for the initial 10 discharge/charge cycles, the NHGHSs can maintain good capacity retention when cycling at the high discharge/charge rates, ranging from 1 to 20 C, and capacities of ~1200 and ~1560 mAh g^{-1} can be recovered once the discharge/charge rates are restored to the initial 1 and 0.5 C, respectively. These results strongly suggest the high stability of the NHGHSs, which can retain their structural integrity despite the repetitive Li$^+$ ion detercalation and intercalation. This can be further demonstrated by the fact that the NHGHS electrode can still deliver a specific capacity of 1643 mAh g^{-1} at the 100 mA g^{-1} after 50 discharge/charge cycles, as shown in Figure 5b. The results shown above strongly suggest that the NHGHSs can be used as an excellent anode material for LIBs with both high energy and power densities. Their superior electrochemical performance

could be attributed to their greatly improved specific surface area as demonstrated above and nitrogen-doped graphene structure, both of which can increase rate capacity and energy density of the NHGHSs. It can be clearly seen that at the relatively low rates the discharge/charge capacities of the NHGHSs are mainly contributed from those below 0.5 V (Figure 5a,c). Previous reports have attributed the capacitance below and above 0.5 V to Li$^+$ ion intercalation into graphene layer and the faradic capacitance on the surface or the edge sites of graphene nanosheets, respectively.[18,49,52] The large capacity contribution below 0.5 V as shown in Figure 5a,c therefore indicates that the large specific surface area demonstrated above plays an important role in the electrochemical performance improvement of the NHGHSs. The nitrogen doping could also be an additional factor for improving the electrochemical performance of the NHGHSs. Since doping can increase the electronic conductivity of NG due to the donation of the lone pair electrons from the N atoms to the graphene π-electron system, and the presence of pyridinic N can increase the adsorption energy and decrease energy barrier for Li$^+$ ion penetration,[35,36] the NHGHSs can thus exhibit enhanced electrochemical performance as the anode materials for the LIB applications. This can be further demonstrated by the facts that the NHGHSs exhibit an increased Coulombic efficiency of the initial discharge/charge cycle (66.9%) compared to the pristine graphene and other graphene-based carbonaceous materials reported in the literature[12,38] and deliver larger discharge/charge capacities at the different discharge/charge rates compared to NGHSs (Figure 5d), due to their higher atom percentage of N (particularly pyridinic N) as demonstrated above.

Indeed, except for those mentioned above, their specific microspherical hollow structure with the walls consisting of NHG could be an additional factor that improves the electrochemical performance of the NHGHSs. The holey structure can not only produce more defect and edge sites that are active for the Li$^+$ ion adsorption but also decrease the interlayer interaction and increase interlayer spacing between the NHG nanosheets in the hollow walls of the NHGHSs (as demonstrated above), which could increase the storage capacity of the NHGHSs, as reported by Honma et al.[18] Furthermore, the hollow structure may work as a reservoir for the ion storage, similar to electrochemical supercapacitors,[53] which allows for the storage of more Li$^+$ ions and consequently higher

electrochemical performance of LIBs. This might explain why the NHGHSs can exhibit an initial discharge capacity of 1923 mAh g^{-1}, a capacity that is ~5 times greater than the theoretical capacity of graphite (372 mAh g^{-1}). Additionally, the increased interlayer spacing between the NHG nanosheets and the holey structure of NHG could also allow the cross-plane diffusion of electrolytes through NHG. This, along with their micro-spherical hollow structure, which makes more active materials accessible to electrolytes and diffusion of electrolytes in and out of the electrode much easier, would result in better utilization of the graphene materials, easier ion diffusion, and electron transfer, and thereby better electrochemical performance of the NHGHSs. To demonstrate this, the EIS spectra of both the NHGHSs and NGHSs are measured, as shown in Figure 6a. The Nyquist plots obtained are then modeled and interpreted using the electrical equivalent circuit shown in the inset of Figure 6a. It reveals that the NHGHSs exhibit much lower electrolyte resistance (R_Ω = 2.79 Ω) and charge transfer resistance (R_{ct} = 21.76 Ω) than the NGHSs (R_Ω and R_{ct} for the NGHSs are 3.26 Ω and 93.13 Ω, respectively), indicating that the NHGHSs allow much easier ion diffusion and electron transfer. The lower electrolyte resistance could be attributed to their specific holey structure of NG and the microspherical hollow structure of the NHGHSs, which allows the cross-plane diffusion of electrolyte through NHG and easier diffusion of electrolytes in and out of the electrode, while the lower charge transfer resistance could be ascribed to the presence of more N doping atoms and the larger surface area of the NHGHSs, leading to higher electrical conductivity of the NHGHSs due to the electron-donating effect of the nitrogen atom and a larger electrolyte−electrode contact area. Indeed, as shown in Figure 6a, the easier diffusion of electrolyte in the NHGHSs can also be demonstrated by the steeper slope of the straight line in the low-frequency region of their Nyquist plot shown in Figure 6a, which is assigned to the solid-state diffusion of the Li$^+$ ion in the electrodes.

The usability of the NHGHSs is further evaluated by the Ragone plot shown in Figure 6b, in which the power and energy densities of the NHGHSs based on the single-electrode weight of the active materials are calculated. For comparison, the results for the NGHSs are also presented in Figure 6b. The energy density E and power density P in a constant current discharge/charge process are calculated using the following equations, respectively:

$$E = \int \frac{IV}{m} dt \tag{1}$$

$$P = \frac{1}{t} \int_0^t \frac{IV}{m} dt \tag{2}$$

where I, V, m, and t correspond to the current, voltage, mass of active material, and charge time of a Li/NHGHS cell, respectively. Figure 6b clearly shows that the NHGHSs deliver much higher energy and power densities than the NGHSs, which is in good agreement with results shown above, which indicate that the NHGHSs exhibit higher electrochemical performance than the NGHSs. Indeed, as shown in Figure 6b, at the discharge/charge rate of 1 C, the NHGHSs can deliver a maximum energy density of 637.4 Wh kg^{-1} with a power density of 182.4 W kg^{-1}, even at the higher rate of 20 C, the NHGHSs can still deliver a maximum energy density of 445.3 Wh kg^{-1} with a power density of 12.86 kW kg^{-1}. The energy and power densities of the NHGHSs are much higher than

other carbonaceous materials,[3,54−56] which clearly demonstrate the great potential of using the NHGHSs in the practical LIBs applications. The great potential of using the NHGHSs as the anode for LIBs can be further demonstrated by their higher volumetric capacity density (~86.05 mAh cm^{-3}, estimated based on their tap density mentioned in the Experimental Section) than those of other graphene-based carbonaceous materials reported previously (<40 mAh cm^{-3}, calculated based on their reported tap densities).[12,57]

CONCLUSIONS

In summary, the NHGHSs have been synthesized through the template sacrificing method. These NHGHSs can exhibit substantially high electrochemical performance when used as the anode material for LIBs, such as high energy and power densities, good reversibility, and excellent cycling stability. Their attractive electrochemical performance could be attributed to their specific structure, which consists of NHG assembled in the microspherical hollow morphology. The nitrogen doping improves the electronic conductivity of the NHGHSs, increases their adsorption energy, and decreases the energy barrier for Li$^+$ ion penetration. The holey structure of NHG provides the NHGHSs with more defect and edge sites for Li$^+$ ion adsorption and allows for the cross-plane diffusion of electrolytes through NHG. These, in combination with its specific microspherical hollow structure and the increased interlayer spacing of the NHG nanosheets in their walls of the hollow structure, give the NHGHSs a high specific surface area and easier accessibility to electrolytes, allowing for a larger reversible capacity for Li$^+$ ion adsorption and faster diffusion of electrolyte into and out of electrode. The results presented therefore demonstrate a new approach to produce LIBs with both higher energy and power densities.

ASSOCIATED CONTENT

Ⓢ Supporting Information
This file provides more detailed information regarding certain experimental procedures for the synthesis of amine-function-alized mesoporous silica nanoparticles (AFMSNs) and graphene oxide, additional information on SEM image of HGO/AFMSNs, and Raman spectra of GO, HGO, NGHS, and NHGHS. This material is available free of charge via the Internet at http://pubs.acs.org.

AUTHOR INFORMATION

Corresponding Author
*E-mail: zhongjiejiang1978@hotmail.com or eszjiang@scut.edu.cn. Phone: +86-020-39381202.
Author Contributions
The manuscript was written through contributions of all authors. All authors have given approval to the final version of the manuscript.
Notes
The authors declare no competing financial interest.

ACKNOWLEDGMENTS

■ REFERENCES

(1) Wu, H.; Yu, G.; Pan, L.; Liu, N.; McDowel, M. T.; Bao, Z.; Cui, Y. Stable Li-ion Battery Anodes by in-situ Polymerization of Conducting Hydrogel to Conformally Coat Silicon Nanoparticles. *Nat. Commun.* **2013**, *4*, 2941(1−6).

(2) Cheng, F.; Liang, J.; Tao, Z.; Chen, J. Functional Materials for Rechargeable Batteries. *Adv. Mater.* **2011**, *23*, 1695−1715.

(3) Mukherjee, R.; Thomas, A. V.; Krishnamurthy, A.; Koratkar, N. Photothermally Reduced Graphene as High-Power Anodes for Lithium-Ion Batteries. *ACS Nano* **2012**, *6*, 7867−7878.

(4) Yu, H.; Zhou, H. High-Energy Cathode Materials (Li_2MnO_3−$LiMO_2$) for Lithium-Ion Batteries. *J. Phys. Chem. Lett.* **2013**, *4*, 1268−1280.

(5) Manthiram, A. Materials Challenges and Opportunities of Lithium Ion Batteries. *J. Phys. Chem. Lett.* **2011**, *2*, 176−184.

(6) Chen, J.; Cheng, F. Combination of Lightweight Elements and Nanostructured Materials for Batteries. *Acc. Chem. Res.* **2009**, *42*, 713−723.

(7) Han, S.; Wu, D.; Li, S.; Zhang, F.; Feng, X. Porous Graphene Materials for Advanced Electrochemical Energy Storage and Conversion Devices. *Adv. Mater.* **2014**, *26*, 849−864.

(8) Varzi, A.; Bresser, D.; Zamory, J. v.; Müller, F.; Passerini, S. $ZnFe_2O_4$-C/$LiFePO_4$-CNT: A Novel High-Power Lithium-Ion Battery with Excellent Cycling Performance. *Adv. Energy Mater.* **2014**, *4*, 1400054(1−9).

(9) Lee, W. J.; Hwang, T. H.; Hwang, J. O.; Kim, H. W.; Lim, J.; Jeong, H. Y.; Shim, J.; Han, T. H.; Kim, J. Y.; Choi, J. W.; Kim, S. O. N-Doped Graphitic Self-Encapsulation for High Performance Silicon Anodes in Lithium-Ion Batteries. *Energy Environ. Sci.* **2014**, *7*, 621−626.

(10) Jiang, Z.; Pei, B.; Manthiram, A. Randomly Stacked Holey Graphene Anodes for Lithium Ion Batteries with Enhanced Electrochemical Performance. *J. Mater. Chem. A* **2013**, *1*, 7775−7781.

(11) Zhao, X.; Hayner, C. M.; Kung, M. C.; Kung, H. H. Flexible Holey Graphene Paper Electrodes with Enhanced Rate Capability for Energy Storage Applications. *ACS Nano* **2011**, *5*, 8739−8749.

(12) Wu, Z.-S.; Ren, W.; Xu, L.; Li, F.; Cheng, H.-M. Doped Graphene Sheets as Anode Materials with Superhigh Rate and Large Capacity for Lithium Ion Batteries. *ACS Nano* **2011**, *5*, 5463−5471.

(13) Reddy, A. L. M.; Srivastava, A.; Gowda, S. R.; Gullapalli, H.; Dubey, M.; Ajayan, P. M. Synthesis of Nitrogen-Doped Graphene Films for Lithium Battery Application. *ACS Nano* **2010**, *4*, 6337−6342.

(14) Gong, Y.; Yang, S.; Liu, Z.; Ma, L.; Vajtai, R.; Ajayan, P. l. M. Graphene-Network-Backboned Architectures for High-Performance Lithium Storage. *Adv. Mater.* **2013**, *25*, 3979−3984.

(15) Gwon, H.; Kim, H.-S.; Lee, K. U.; Seo, D.-H.; Park, Y. C.; Lee, Y.-S.; Ahn, B. T.; Kang, K. Flexible Energy Storage Devices Based on Graphene Paper. *Energy Environ. Sci.* **2011**, *4*, 1277−1283.

(16) Chen, D.; Tang, L.; Li, J. Graphene-Based Materials in Electrochemistry. *Chem. Soc. Rev.* **2010**, *39*, 3157−3180.

(17) Yao, F.; Gunes, F.; Ta, H. Q.; Lee, S. M.; Chae, S. J.; Sheem, K. Y.; Cojocaru, C. S.; Xie, S. S.; Lee, Y. H. Diffusion Mechanism of Lithium Ion Through Basal Plane of Layered Graphene. *J. Am. Chem. Soc.* **2012**, *134*, 8646−8654.

(18) Yoo, E.; Kim, J.; Hosono, E.; Zhou, H.-s.; Kudo, T.; Honma, I. Large Reversible Li Storage of Graphene Nanosheet Families for Use in Rechargeable Lithium Ion Batteries. *Nano Lett.* **2008**, *8*, 2277−2282.

(19) Pan, D.; Wang, S.; Zhao, B.; Wu, M.; Zhang, H.; Wang, Y.; Jiao, Z. Li Storage Properties of Disordered Graphene Nanosheets. *Chem. Mater.* **2009**, *21*, 3136−3142.

(20) Stoller, M. D.; Park, S.; Zhu, Y.; An, J.; Ruoff, R. S. Graphene-Based Ultracapacitors. *Nano Lett.* **2008**, *8*, 3498−3502.

(21) Vu, A.; Qian, Y.; Stein, A. Porous Electrode Materials for Lithium-Ion Batteries − How to Prepare Them and What Makes Them Special. *Adv. Energy Mater.* **2012**, *2*, 1056−1085.

(22) Xiao, J.; Mei, D.; Li, X.; Xu, W.; Wang, D.; Graff, G. L.; Bennett, W. D.; Nie, Z.; Saraf, L. V.; Aksay, I. A.; Liu, J.; Zhang, J. G. Hierarchically Porous Graphene as A Lithium-Air Battery Electrode. *Nano Lett.* **2011**, *11*, 5071−5078.

(23) Li, Y.; Fu, Z.-Y.; Su, B.-L. Hierarchically Structured Porous Materials for Energy Conversion and Storage. *Adv. Funct. Mater.* **2012**, *22*, 4634−4667.

(24) Winter, M.; Besenhard, J. O.; Spahr, M. E.; Novák, P. Insertion Electrode Materials for Rechargeable Lithium Batteries. *Adv. Mater.* **1998**, *10*, 725−763.

(25) Matsumura, Y.; Wang, S.; Mondori, J. Interactions Between Disordered Carbon and Lithium in Lithium Ion Rechargeable Batteries. *Carbon* **1995**, *33*, 1457−1462.

(26) Poh, H. L.; Šimek, P.; Sofer, Z.; Pumera, M. Sulfur-Doped Graphene via Thermal Exfoliation of Graphite Oxide in H_2S, SO_2, or CS_2 Gas. *ACS Nano* **2013**, *7*, 5262−5272.

(27) Wang, H.; Zhang, C.; Liu, Z.; Wang, L.; Han, P.; Xu, H.; Zhang, K.; Dong, S.; Yao, J.; Cui, G. Nitrogen-Doped Graphene Nanosheets with Excellent Lithium Storage Properties. *J. Mater. Chem.* **2011**, *21*, 5430−5434.

(28) Yin, S.; Zhang, Y.; Kong, J.; Zou, C.; Li, C. M.; Lu, X.; Ma, J.; Boey, F. Y. C.; Chen, X. Assembly of Graphene Sheets into Hierarchical Structures for High-Performance Energy Storage. *ACS Nano* **2011**, *5*, 3831−3838.

(29) Zhou, L.-J.; Hou, Z. F.; Wu, L.-M. First-Principles Study of Lithium Adsorption and Diffusion on Graphene with Point Defects. *J. Phys. Chem. C* **2012**, *116*, 21780−21787.

(30) Kattel, S.; Atanassov, P.; Kiefer, B. Stability, Electronic and Magnetic Properties of In-Plane Defects in Graphene: A First-Principles Study. *J. Phys. Chem. C* **2012**, *116*, 8161−8166.

(31) Fan, X.; Zheng, W. T.; Kuo, J.-L. Adsorption and Diffusion of Li on Pristine and Defective Graphene. *ACS Appl. Mater. Interfaces* **2012**, *4*, 2432−2438.

(32) Das, D.; Kim, S.; Lee, K.-R.; Singh, A. K. Li Diffusion Through Doped and Defected Graphene. *Phys. Chem. Chem. Phys.* **2013**, *15*, 15128−15134.

(33) Pan, D.; Wang, S.; Zhao, B.; Wu, M.; Zhang, H.; Wang, Y.; Jiao, Z. Li Storage Properties of Disordered Graphene Nanosheets. *Chem. Mater.* **2009**, *21*, 3136−3142.

(34) Hu, C.; Xiao, Y.; Zhao, Y.; Chen, N.; Zhang, Z.; Cao, M.; Qu, L. Highly Nitrogen-Doped Carbon Capsules: Scalable Preparation and High-Performance Applications in Fuel Cells and Lithium Ion Batteries. *Nanoscale* **2013**, *5*, 2726−2733.

(35) Yu, Y.-X. Can All Nitrogen-Doped Defects Improve the Performance of Graphene Anode Materials for Lithium-Ion Batteries? *Phys. Chem. Chem. Phys.* **2013**, *15*, 16819−16827.

(36) Ma, C.; Shao, X.; Cao, D. Nitrogen-Doped Graphene Nanosheets as Anode Materials for Lithium Ion Batteries: A First-Principles Study. *J. Mater. Chem.* **2012**, *22*, 8911−8915.

(37) Hu, T.; Sun, X.; Sun, H.; Xin, G.; Shao, D.; Liu, C.; Lian, J. Rapid Synthesis of Nitrogen-Doped Graphene for A Lithium Ion Battery Anode with Excellent Rate Performance and Super-Long Cyclic Stability. *Phys. Chem. Chem. Phys.* **2014**, *16*, 1060−1066.

(38) He, C.; Wang, R.; Fu, H.; Shen, P. K. Nitrogen-Self-Doped Graphene as A High Capacity Anode Material for Lithium-Ion Batteries. *J. Mater. Chem. A* **2013**, *1*, 14586−14591.

(39) Hummers, W. S.; Offeman, R. E. Preparation of Graphitic Oxide. *J. Am. Chem. Soc.* **1958**, *80*, 1339−1339.

(40) Zhang, F.; Zhang, T.; Yang, X.; Zhang, L.; Leng, K.; Huang, Y.; Chen, Y. A High-Performance Supercapacitor-Battery Hybrid Energy Storage Device Based on Graphene-Enhanced Electrode Materials with Ultrahigh Energy Density. *Energy Environ. Sci.* **2013**, *6*, 1623.

(41) Hennrich, F.; Krupke, R.; Arnold, K.; Stütz, J. A. R.; Lebedkin, S.; Koch, T.; Schimmel, T.; Kappes, M. M. The Mechanism of Cavitation-Induced Scission of Single-Walled Carbon Nanotubes. *J. Phys. Chem. B* **2007**, *111*, 1932−1937.

(42) Wang, S.; Tang, L. A.; Bao, Q.; Lin, M.; Goh, S. B. M.; Loh, K. P. Room-Temperature Synthesis of Soluble Carbon Nanotubes by the

19090

dx.doi.org/10.1021/am5050604 | *ACS Appl. Mater. Interfaces* 2014, 6, 19082−19091

Sonication of Graphene Oxide Nanosheets. *J. Am. Chem. Soc.* **2009**, *131*, 16832−16837.

(43) Mason, T. J.; Lorimer, J. P. *Sonochemistry: Theory, Applications and Uses of Ultrasound in Chemistry*; Ellis Horwood: New York, 1988.

(44) Jiang, Z.; Shi, Y.; Jiang, Z.-J.; Tian, X.; Luo, L.; Chen, W. High Performance of Free-Standing Sulfonic Acid Functionalized Holey Graphene Oxide Paper as a Proton Conducting Polymer Electrolyte for Air-Breathing Direct Methanol Fuel Cells. *J. Mater. Chem. A* **2014**, *2*, 6494−6503.

(45) Liu, J.; Rinzler, A. G.; Dai, H.; Hafner, J. H.; Bradley, R. K.; Boul, P. J.; Lu, A.; Iverson, T.; Shelimov, K.; Huffman, C. B.; Rodriguez-Macias, F.; Shon, Y.-S.; Lee, T. R.; Colbert, D. T.; Smalley, R. E. Fullerene Pipes. *Science* **1998**, *280*, 1253−1256.

(46) Ju, H.-M.; Choi, S.-H.; Huh, S. H. X-ray Diffraction Patterns of Thermally-reduced Graphenes. *J. Korean Phys. Soc.* **2010**, *57*, 1649−1652.

(47) Lin, Z.; Song, M. K.; Ding, Y.; Liu, Y.; Liu, M.; Wong, C. P. Facile Preparation of Nitrogen-Doped Graphene as A Metal-Free Catalyst for Oxygen Reduction Reaction. *Phys. Chem. Chem. Phys.* **2012**, *14*, 3381−3387.

(48) Huang, Y.; Liang, J.; Chen, Y. An Overview of the Applications of Graphene-Based Materials in Supercapacitors. *Small* **2012**, *12*, 1805−1834.

(49) Lian, P.; Zhu, X.; Liang, S.; Li, Z.; Yang, W.; Wang, H. Large Reversible Capacity of High Quality Graphene Sheets as An Anode Material for Lithium-Ion Batteries. *Electrochim. Acta* **2010**, *55*, 3909−3914.

(50) Vinayan, B. P.; Nagar, R.; Raman, V.; Rajalakshmi, N.; Dhathathreyan, K. S.; Ramaprabhu, S. Synthesis of Graphene-Multiwalled Carbon Nanotubes Hybrid Nanostructure by Strengthened Electrostatic Interaction and Its Lithium Ion Battery Application. *J. Mater. Chem.* **2012**, *22*, 9949−9956.

(51) Wang, G.; Shen, X.; Yao, J.; Park, J. Graphene Nanosheets for Enhanced Lithium Storage in Lithium Ion Batteries. *Carbon* **2009**, *47*, 2049−2053.

(52) Wang, C.; Li, D.; Too, C. O.; Wallace, G. G. Electrochemical Properties of Graphene Paper Electrodes Used in Lithium Batteries. *Chem. Mater.* **2009**, *21*, 2604−2606.

(53) Wang, G.; Zhang, L.; Zhang, J. A Review of Electrode Materials for Electrochemical Supercapacitors. *Chem. Soc. Rev.* **2012**, *41*, 797−828.

(54) Jang, B. Z.; Liu, C.; Neff, D.; Yu, Z.; Wang, M. C.; Xiong, W.; Zhamu, A. Graphene Surface-Enabled Lithium Ion-Exchanging Cells: Next-Generation High-Power Energy Storage Devices. *Nano Lett.* **2011**, *11*, 3785−3791.

(55) Ha, S. H.; Jeong, Y. S.; Lee, Y. J. Free Standing Reduced Graphene Oxide Film Cathodes for Lithium Ion Batteries. *ACS Appl. Mater. Interfaces* **2013**, *5*, 12295−12303.

(56) Hossain, S.; Kim, Y.-K.; Saleh, Y.; Loutfy, R. Overcharge Studies of Carbon Fiber Composite-Based Lithium-Ion Cells. *J. Power Sources* **2006**, *161*, 640−647.

(57) Zhang, B.; Yu, Y.; Liu, Y.; Huang, Z.-D.; He, Y.-b.; Kim, J.-K. Percolation Threshold of Graphene Nanosheets as Conductive Additives In $Li_4Ti_5O_{12}$ Anodes of Li-Ion Batteries. *Nanoscale* **2012**, *5*, 2100−2106.